Article
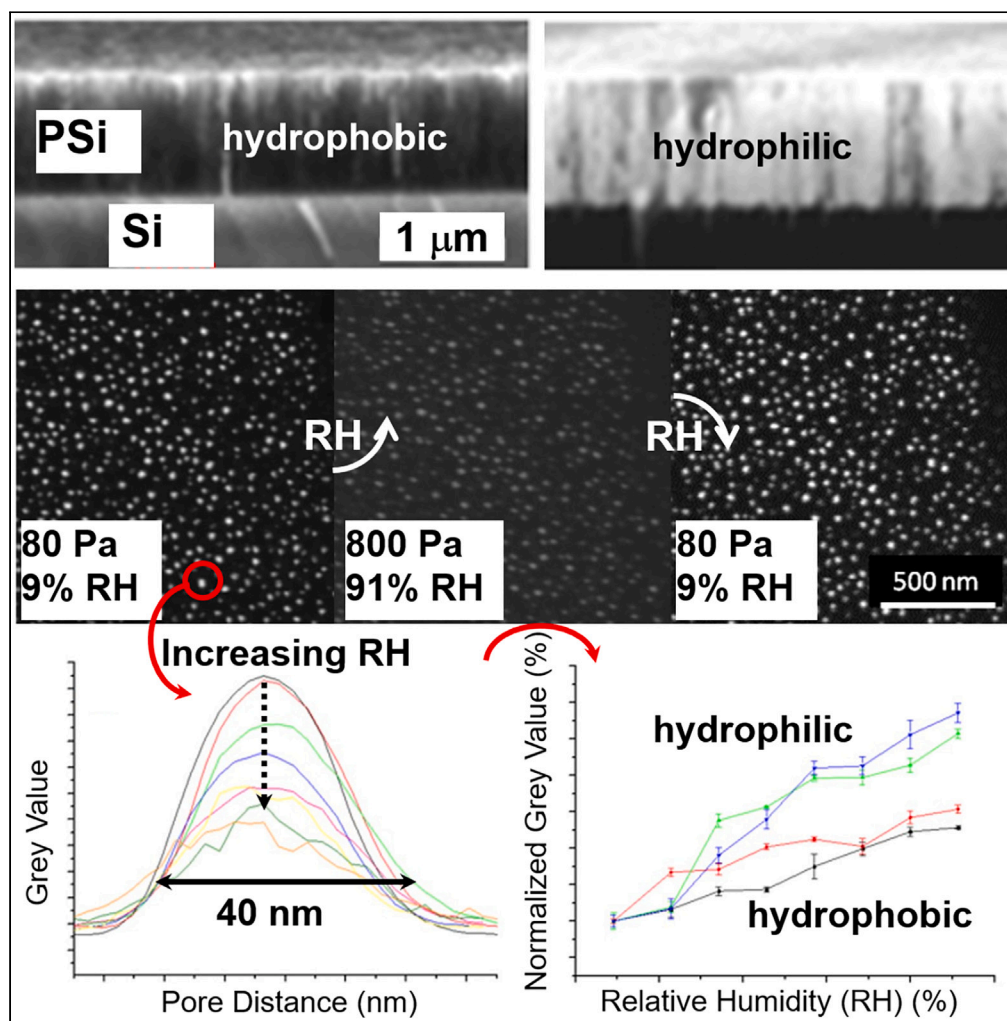
Electron microscopy approach to the wetting dynamics of single organosilanized mesopores

C. Rodriguez, V.
Torres-Costa, A.M.
Bittner, ..., E.
Modin, A. Chuvilin,
M. Manso Silván

miguel.manso@uam.es

Highlights

Wetting studied by
wetSTEM in size
categorized silicon
mesopores

Gray scale profile in pores
changes as a function of
relative humidity and
chemistry

Isotherms constructed by
averaging gray scale by
pore size categories

Isotherms correlate with
global wetting on
hydrophilic-phobic
mesopores

Article

Electron microscopy approach to the wetting dynamics of single organosilanized mesopores

C. Rodriguez,[1,2] V. Torres-Costa,[1] A.M. Bittner,[3,4] S. Morin,[3,5] M. Cascajo Castresana,[3,6] S. Chiriaev,[7] E. Modin,[3] A. Chuvilin,[3,4] and M. Manso Silván[1,8,*]

SUMMARY

Columnar mesoporous silicon (PSi) with hydrophobic vs. hydrophilic chemistries was chosen as a model for the local (pore-by-pore) study of water-pore interactions. Tomographic reconstructions provided a 3D view of the ramified pore structure. An *in situ* study of PSi wetting was conducted for categorized pore diameters by environmental scanning TEM. An appropriate setting of the contrast allows for the normalization of the gray scale in the images as a function of relative humidity (RH). This allows constructing an isotherm for each single pore and a subsequent averaging provides an isotherm for each pore size range. The isotherms systematically point to an initial adsorption through the formation of water adlayers, followed by a capillary filling process at higher RH. The local isotherms correlate with (global) gravimetric determination of wetting. Our results point at the validation of a technique for the study of aging and stability of single-pore nanoscale devices.

INTRODUCTION

The study of the adsorption of water in porous media provides information about the nature of the interaction between the porous matrix and water vapor. In restricted geometries, water molecules can interact with surfaces through hydrophobic, hydrophilic, and hydrogen-bond interactions. These interactions are governed by the interplay between the strength of surface-liquid and liquid-liquid interactions as well as by the effects of confined pore space on the state and thermodynamic stability of the liquid. A confined pore space can lead to interesting new structures of water that differ from wetting patterns on flat surfaces. In addition, confined water has properties that are not observed in bulk water.[1] This is the case for water molecules enclosed in zeolites, cements, or in hydration shells of proteins.[2,3] These examples motivate a wide applicability of wetting studies in materials, but also in the study of biological processes and in biosensing. In a simplified model, there are two types of water configurations in pores,[3] free water (water on water, no contact with the pore wall) and water confined at the pore material interface (at the pore wall) as established by experimental techniques such as NMR (of zeolites[1] and granite residual soils,[4] using T2 relaxometry mode in this latter case) and X-ray tomography (of glass beads[5] or granite residual soils[6]). Relevantly, the sensitivity of these techniques allows providing details of the changes induced in the pores after cyclic wetting and drying. The structure observed for water confined in pores is analogous to the complex case of hydration of proteins.

Water vapor adsorption in porous media, and in particular, evaporation/condensation from porous silicon (PSi) in response to variations in ambient conditions, is used in many technological applications such as drying, separation, catalytic reactions, optoelectronics, and biomedicine.[7] It is also critical for the protection of PSi based devices. Indeed, high environmental humidity can affect their performance and reliability by changing their optical and/or electrical properties as briefly reviewed in Table 1. Surface functionalization is a logical step for the protection of devices and has been extensively applied to PSi surfaces.[8,9]

The use of self-assembled organosilane layers is an effective approach to control humidity effects. In fact, organosilanes have attracted significant attention due to their tunable surface properties to control wetting or biocompatibility in homogeneous and micro-patterned areas.[16] By employing organosilanes with different terminal groups, the surface can be engineered to attract or repel water. In biotechnology, the wetting characteristics of organosilane-modified surfaces are the main factor affecting the protein adsorption on a biomaterial.[17] The adsorption of proteins, including proteins on bacterial surfaces, is responsible for biocompatibility, biofouling, and all other interface-dependent properties. Understanding the wetting ability of biomaterial surfaces at the microscopic scale is therefore of primary importance. We aim

[1]Departamento de Física Aplicada, Centro de Microanálisis de Materiales and Instituto Nicolás Cabrera, Universidad Autónoma de Madrid, 28049 Madrid, Spain
[2]Mecwins, Roda de Poniente 15, Tres Cantos, Madrid 28760, Spain
[3]CIC nanoGUNE, 20018 Donostia-San Sebastián, Spain
[4]Ikerbasque, Basque Foundation for Science, 48013 Bilbao, Spain
[5]Department of Chemistry, York University, 4700 Keele Street, Toronto M3J 1P3, Canada
[6]Tecnalia, 20009 Donostia-San Sebastián, Spain
[7]Mads Clausen Institute, University of Southern Denmark, 6400 Sønderborg, Denmark
[8]Lead contact
*Correspondence: miguel.manso@uam.es
https://doi.org/10.1016/j.isci.2023.107981

Table 1. Effect of relative humidity (RH) on the basic electrical and optical properties of PSi

	Property	Response to increasing RH	Reference
Electrical	Conductance	Increase	Mares et al.[10]
	Impedance	None	Kovacs et al.[11]
	Capacity	Increase	Rittersma et al.[12]
Optical	Reflectivity	Decrease	Xifré Pérez et al.[13]
	Photoluminescence	Decrease	Oswald et al.[14] Mandal et al.[15]

at expanding the research on material surfaces from standard flat models to real porous surfaces, including the complex geometry in PSi. Free standing layers of columnar PSi are the samples of choice for such in-depth characterization.

Environmental scanning transmission electron microscopy (wetSTEM) is a technique that enables real time and real space observations of wet samples with nm resolution, including imaging of liquid water on complex surfaces, even into pores. The sample environment can be controlled by independently adjusting the water vapor pressure and the sample temperature in the electron microscope sample chamber.[18,19] Several types of nanostructures (metallic, inorganic, and organic) have been observed in wetSTEM with good resolution and contrast,[18,20] including biological specimens,[18,21] which are low in atomic number and sensitive to beam damage and dehydration. Because specimens can be imaged without dehydration or coating, wetSTEM is of special relevance for biological applications and for biomaterials.

In the present work, we use wetSTEM to study the interaction of water with organosilane-modified PSi. We aim more precisely at describing the different wetting dynamics of PSi layers following a pore-by-pore approach at scaled relative humidity gaps. This implies on the one hand a detailed pre-characterization of the system, performed through complementary microscopic techniques, and on the other hand, the development of a protocol for image acquisition under controlled wetting conditions. Free-standing layers of columnar PSi have been chosen in view of their compatibility with transmission observations and their technological relevance.

RESULTS

Properties of the thin porous silicon layers

The FESEM cross-section image (Figure 1A) shows a general view of the structure of the PSi obtained after electrochemical etching prior to delamination. The characteristic columnar pore anisotropy of these materials can be inferred. A higher magnification HIM image from the PSi/silicon interface shows a transversal cut of superposed parallel pores (Figure 1B). The image was obtained at a landing ion energy of 30 keV. During the imaging scans, we kept the beam current well below 1.0 pA to avoid possible image artifacts related to radiation damage produced by helium ions. The pore walls seen in the image present a rather rugged internal surface, which contains diagonal dendritic features, denoting pore interconnectivity.

Top view imaging of the pores (Figure 1C) shows the microstructure of the free-standing PSi. These TEM images highlight the alignment of the pores and allow determining the pore size distribution. The resulting pore size histogram is shown in Figure 1D, revealing a mean pore size of (40 ± 10) nm.

The functionalization of the samples allowed obtaining surfaces with different hydrophobic/hydrophilic properties. Figure 2 summarizes the surface termination scheme, water contact angles, and PTA infiltration results for the different PSi samples. The values of the contact angles obtained are different from those that would be obtained on flat Si. Indeed, pores and other roughness features play an important role in the apparent surface area of the materials, which in turn influences the contact angles.[22,23] The APTS-functionalized and chemically oxidized PSi surfaces become more hydrophilic when the pores are formed (0° and 22° for our porous structures, as compared to 29° and 49° for flat surfaces, respectively).[24,25] Such variation can be described by the Wenzel model assuming that the water permeates the pores. Meanwhile, the PFDS-functionalized surface becomes more hydrophobic with respect to the flat model (up to 117° for PSi from 88° for the flat Si)[26] and can be described in this case with the Cassie-Baxter model. PFDS-PSi shows approximately the same hydrophobic behavior as the PSi surface covered by SiH$_x$ species after HF treatment (contact angle of ~120°).[23] In passing we note that such contact angles for freshly formed PSi are common for processes not involving silicon oxidative agents and not affected by atmospheric exposure aging.[27,28] The main contribution of the perfluorinated surface in the current study is thus providing a stable hydrophobic behavior, which is not ensured by the Si-H surface of the freshly formed PSi. An estimation obtained by using the Cassie-Baxter equation predicts that the surface area of the hydrophobic PSi samples is composed of ~50% air (pores) and ~50% solid (silicon). To further deepen into the estimation of the fraction of air on the surface we performed a PTA staining experiment by SEM.

The permeation of aqueous PTA solutions was reliably imaged by SEM (Figure 2C). PTA readily dissociates in water to produce anionic species; their chemistry is dominated by the outermost OH and O$^-$ groups, thus they are highly hydrophilic. The PTA staining of biological samples for TEM characterization is indeed based on PTA binding to cationic and hydrophilic surfaces, so we expected a high affinity of PTA to OH-PSi, and especially to APTS-PSi (where the terminal NH$_2$ groups form NH$_3^+$ in water). For these two hydrophilic samples, the complete length of the pores is filled up with PTA, indicating that the pores are permeable, even on the original Si substrate with an occluded pore at the bottom. For H-PSi and PFDS-PSi, which have hydrophobic pore surfaces, the aqueous PTA remains on the top of the porous structure.
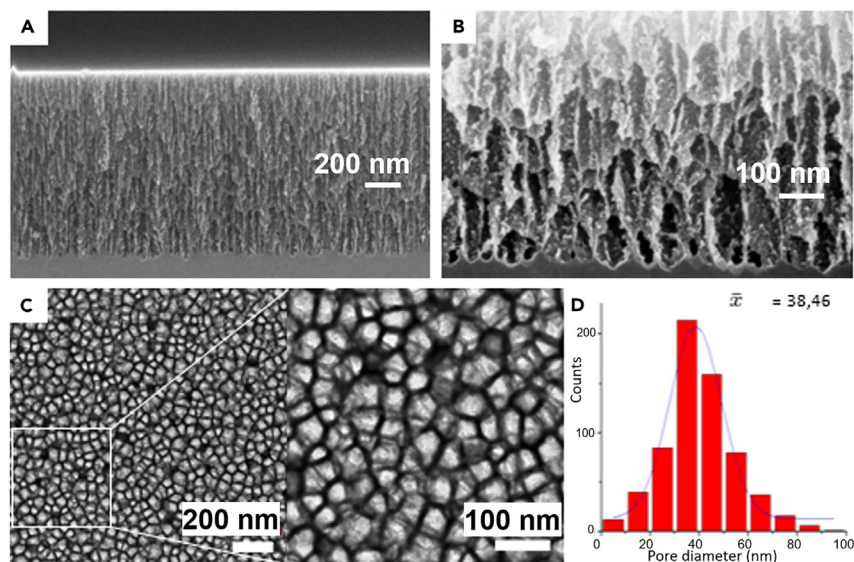
**Figure 1. Electron microscopy characterization of columnar PSi**

(A–D) Cross section scanning electron microscopy image of columnar PSi, (B) Helium ion microscopy magnification of the pores in a cross section imaged at the interface with Si (C) transmission electron microscopy top planar view of the general pore distribution of free-standing PSi, and (D) Pore diameter distribution obtained from image c.

Using the permeation of PTA approach described above, we also realized FIB tomography imaging. These measurements were performed on an APTS-PSi sample (Figure 3). Figure 3 a shows the in-depth 3D reconstruction of the structure from a top view section of approximately 3 × 3 μm² area and 2 μm depth. It should be noted that the water (PTA) reaches the bottom of the sample over the whole imaged volume. This agrees with the previous SEM results (Figure 2C). From the top surface, the whole slice shows a diversity of conical tracks opening to the bottom. Visualization of such cones suggests the presence of pores of different permeability, which agrees with the observation of a distribution of pore sizes at the surface, as observed by TEM. Furthermore, higher magnification tomography images from isolated surface pores allowed reconstructing the structure of PSi pores, which is dendritic and open (Figure 3B). In particular, a root-like structure is observed with pores spreading horizontally and converging vertically at deeper levels. This pore-by-pore reconstruction is coherent with the observation of the conical structures, denoting that bigger pores act as "funnels" for PTA distribution. In other words, the fastest way to refill the bottom of the pores is not necessarily the pore immediately on top at the surface. The area of influence of funnel-like surface pores at the surface extends circa 0.8 μm radially at the bottom of the PSi surface. Since the porosity is open and ramified, this area of influence cannot be considered exclusive. These results compare very well with the HIM data, which already suggest topographically the presence of a dendritic pore structure. Note that HIM reveals the pore wall microstructure, while PTA staining provides a 3D view of pore interconnectivity and clearly illustrates that there is margin for molecular flow through this interconnectivity. Relevantly, if the fraction of air in one of the slices is considered, the result is in very good agreement with the 50% estimation obtained from the application of the Cassie-Baxter model to the hydrophobic surfaces.

Condensation/evaporation cycles by environmental scanning transmission electron microscopy

We carried out condensation-evaporation cycles in wetSTEM by increasing and decreasing the chamber pressure and acquiring images at each RH level. We were able to observe gradual water filling of single pores, as seen in Figure 4, clearly identifying RH ranges where water-water nucleation proceeds in individual pores. Relevantly, the PSi structural integrity is not affected by the condensation and evaporation cycles, as we can see in the wetSTEM images of a region of the OH-PSi sample during wetting (Figures 4A–4D) and after drying (Figure 4E). Capillary forces are in fact known to destroy nanoscale structures, so that this stability is key for establishing columnar PSi as a model surface.[28] Analogous series of images were collected for the different types of surface terminations and the electron transmission was analyzed according to pore diameter and vapor pressure. For each type of functionalization at a vapor pressure step, we found only small variations of contrast for pores of similar size, which allowed us obtaining direct visualization of pore refilling according to pore size. The statistics for each size allowed obtaining averages of pore refilling for different categories of pores according to their size in steps of 5 nm.

Figure 5 shows the electron transmission intensity profiles along the diameter of (35 ± 2.5) nm pores. The electron intensity read through the gray value (a high gray value refers to a bright area, and vice-versa) is obtained according to the description in the methods, so that the contrast settings are not modified along the RH conditions of the experiments. The pores are screened on a single-pore basis, for the four types of PSi samples and the different pore size categories in each sample. It is worth outlining that the intensity reaches its maximum close to the center of the pores, but this intensity is not in saturation. Analogous plots were obtained for pores in the 20, 25 and 30 nm ranges (see supplemental information). With all the recovered data we could confirm that the contrast (gray value difference) between dry and wet pores
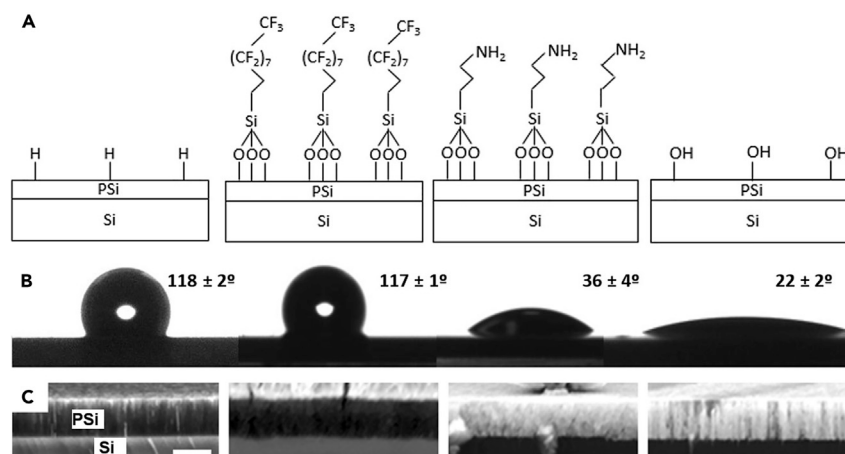
Figure 2. Different surface chemistries and wetting at columnar PSi

(A–C) Schematic of the porous silicon (PSi) surface chemistry for (from left to right): as-formed PSi, Perfluorodecylsilane (PFDS) functionalized PSi, Aminopropyltriethoxysilane (APTS) functionalized PSi and peroxidized PSi, (B) static contact angles of the PSi surfaces and (C) backscattered electron image of the cross-section of the PSi surfaces in presence of Phosphotungstic acid (PTA). From left to right: as-formed PSi, PSi functionalized with PFDS, PSi functionalized with APTS, and peroxidized PSi. Bright contrast in the layer on two right images indicates PTA infiltration. Scale bar is 1 μm.

during the condensation cycle is much lower in the case of H-PSi and PFDS-PSi (on a 256 gray scale level, from 50 to 105 and from 70 to 135, respectively, Figures 5A and 5B) than in the case of APTS-PSi and OH-PSi (from 45 to 160 and from 100 to 210, respectively, Figures 5C and 5D). The observation of these two categories of gray value contrasts differentiated by their maximum yield, may be related to two different sorption behaviors. Indeed, this observation may be associated to competing wetting processes in the mesopores, such as multilayer adsorption and capillary pore condensation mechanisms, respectively.

From the inner pore electron intensity profiles described above, we obtained the maximum gray value for each RH. The data are represented in a normalized inverted scale as shown in Figure 6 and categorized for each pore diameter range (a to d). To obtain the data, a Gaussian fitting of the corresponding pore intensity profiles was used to obtain the gray value at the pore center (maximum gray value) and base gray level for each RH. Normalization consisted in attributing a 100% gray value (black) to the largest gray value at each pore range (always a condition close to the lowest measured RH) and attributing evolving gray values for the increasing RH conditions. The gray scale is inverted to illustrate the increase of adsorption with water pressure, as typically represented in gravimetric isotherms. According to the slope of the plots in Figure 6A–6D we observe a trend based on surface chemistry. On the one hand, OH-PSi and APTS-PSi, whose porous surfaces are easily permeated, show a larger slope. On the other hand, H-PSi and PFDS-PSi, whose surfaces are resistant to water permeation show consistently smaller slopes. For a fixed vapor pressure and considering the dynamics of the adsorption experiment, it can be stated that the mean rate of decrease of the gray value (increase of water permeation) is higher for the hydrophilic PSi samples than for the hydrophobic ones, meaning that the hydrophilic pores are filled more efficiently.

To compile the results obtained for the different pore radii in a rational manner and with a view to potentially different sorption mechanisms we recovered assumptions related to capillary condensation in pores. In fact, this process depends not only on the attraction between water and pore wall, but also on the attractive interactions between the water molecules. At low RH, the pore walls are covered by an adsorbed water multilayer[29] that remains isolated due to the presence of metastable nucleation barriers. When at higher RH the lateral interactions between adsorbed water molecules become stronger than the interactions between the PSi surface and water, nucleation points appear and capillary forces dominate. This is especially the case for the hydrophobic samples but occurs at lower RH for the hydrophilic samples. This can be deduced, in a simplified way, from the Kelvin equation:

$$\ln(\text{RH}) = \ln\frac{P_c}{P_0} = -\frac{2\sigma V_m \cos(\theta_f)}{RTr} \qquad \text{(Equation 1)}$$

which relates the pore condensation pressure P_c (or the relative humidity RH = P_c/P_0) to the pore radius r, and to the contact angle θ_f of the silanized flat Si. Our setup keeps all other parameters constant (P_0 is the vapor pressure of bulk water, σ is the liquid-vapor surface tension, V_m is the molar volume of the liquid, R is the universal gas constant and T is the temperature). For PSi surface with low contact angle, i.e., for the hydrophilic silane layers, the Kelvin equation predicts pore wetting at low RH. For the highest contact angles, close to 90° (for planar models of H-Si and for PFDS) mean that pores fill only at saturation (RH = 100%).

This result agrees with the FESEM cross-section observation of the different PSi samples taken after PTA sorption (Figure 2). We can clearly see that, in the case of the hydrophilic samples, the solution enters the pores over the whole thickness of the layer, contrary to the hydrophobic samples, in which the water/PTA remains at the surface. Therefore, a different filling mechanism can be expected depending on the hydrophilicity of the samples. It is plausible that in hydrophobic samples, the water molecules form aggregates of several molecules instead of being uniformly distributed along the surface. Once a critical cluster size is reached, these aggregates coalesce to produce the condensed
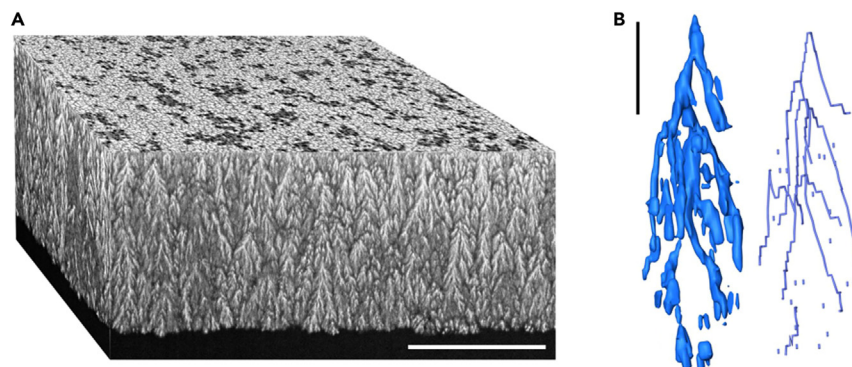
Figure 3. Tomography image of aminopropyl-triethoxysilane functionalized PSi
(A and B) Three-dimensional phosphotungstic-acid enabled tomography images of (a) porous silicon functionalized with aminopropyl-triethoxysilane (scale bar 1000 nm) and (b) a dendrite single-pore structure magnification from the same sample (scale bar 200 nm).

phase.[3] Therefore, the functionalization through perfluorosilanes such as PFDS provides hydrophobic properties[30] and may allow for an increasing stability of the surface against the environment. Capillary condensation mechanisms do happen in both types of hydrophilic and hydrophobic PSi, but close to saturation RH in the case of the hydrophobic ones. In hydrophilic pores, however, the water layer grows homogeneously. This suggests layer-by-layer condensation of water on the pore walls, and the consequent more efficient filling of the pores.[3] This effect was verified for each single pore, while mechanisms are usually deduced from global averages over many pores, which are usually not identical. We believe that our wetSTEM data open the way to a general explanation of capillary filling mechanisms, but also to single-pore devices.

The Kelvin equation (Equation 1) furthermore postulates that pore condensation shifts to higher RH with increasing pore diameter,[31] i.e., smaller pores are preferentially filled. Indeed, we found from many observations of single pores, that electron transmission strongly decreases, translating into increasing filling, for decreasing pore diameters. In the following we show how this effect correlates with macroscopic adsorption measurements.

### Correlated water adsorption measurements

Figure 7 shows the water adsorption and desorption isotherms of the PSi samples as function of RH measured with a Belsorp-Aqua apparatus. These isotherms provide information about the wetting and the hydrophilic or hydrophobic properties of the samples. In the case of adsorption, the curves are monotonous and concave (curving upwards), or type III according to the IUPAC classification.[32]

Upon the necessary change in ordinate scale, the results agree with the wetSTEM measured adsorption, indicating a weak interaction of the water with the PSi surface pointing to condensation by capillarity. Moreover, the amount of water adsorbed is very low for H-PSi and PFDS-PSi and is increased for OH-PSi and APTS-PSi. Indeed, as suggested by the Kelvin equation (Equation 1) which provides a relationship between the pore diameter and the pore condensation pressure (P_c), pore condensation shifts to a higher relative pressure, and consequently to higher RH, with increasing contact angle.
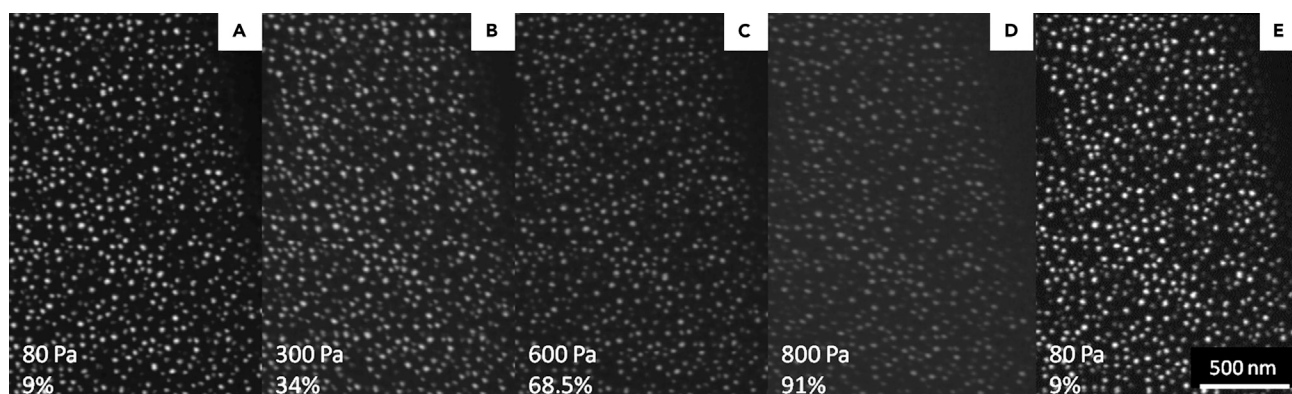
Figure 4. wetSTEM images from peroxidized PSi at increasing humidity and after drying out
(A–E) wetSTEM images from peroxidized free-standing PSi at increasing humidity: (A) 9.1%, (B) 34,2%, (C) 68,5% and (D) 91,3% RH and (E) after drying.
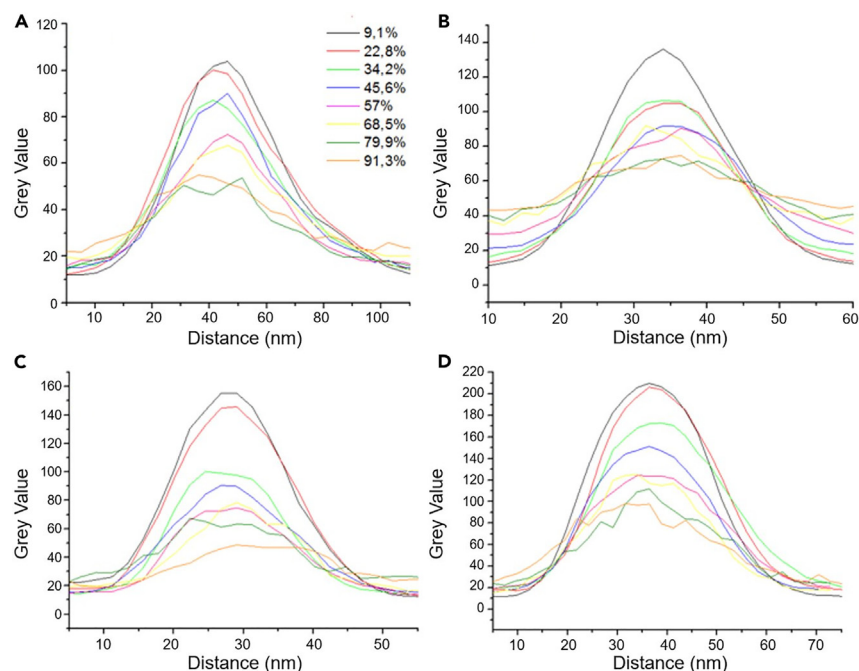
Figure 5. Cross section intensity profiles in categorized pores (35 nm)
(A–D) Pore (d = 35 nm) image intensity profiles at different levels of increasing RH for (A) as-formed PSi, (B) PSi functionalized with PFDS, (C) functionalized with APTS, and (D) peroxidized PSi.

Although H-PSi and PFDS-PSi present almost the same contact angle (118° and 117°, respectively), they exhibit a different amount of adsorbed water. This can be due to the partial oxidation of H-PSi, which can occur in the time span from the etching to the moment of analysis and even during the wetting process in view of the favorable free energy change (enthalpy diminishes and entropy increases by oxidizing H-PSi).

However, contrary to the continuous contrast change obtained from the wetSTEM data (Figure 6), Figure 7 shows that water condensation is enhanced at higher RH (>60% RH). This difference in the influence of RH on the wetSTEM contrast and water adsorption/desorption isotherm is due to the different set of thermodynamic conditions used in both experiments. Indeed, wetSTEM measurements were performed at 5°C over a range of pressures up to 866 Pa, whereas in the case of the gravimetric measurements the analysis was performed at 25°C, reaching a total pressure of 2338 Pa.

Regarding the desorption curves, we also note a different behavior between the hydrophobic and the hydrophilic samples (Figure 7). The former present strongly curved desorption isotherms, indicating the existence of both equilibrium evaporation and pore blocking effects.[31] Indeed, from 90% to ∼20% RH, desorption is associated to the evaporation of liquid from open pores (Figure 7). The observed final step from ∼10% to 0% RH is, however, resulting from the blocked mesopores remaining filled until they empty via cavitation. On the other hand, the more hydrophilic samples also present a desorption curve with a very small slope at low RH, and a very large one at high RH. This typical path of the adsorption isotherm is shown in Figures 7C and 7D. The water adsorption/desorption curves (Figure 7) present a hysteresis, which is a consequence of the presence of pores with alternating wide and narrow parts. The origin of these wide and narrow parts in the pores derives from the general description of the pore structure and the observation that narrower pores refill (so plausibly also desorb) through wider pores. As the partial pressure of saturated water vapor is lowered in the narrower pores, the evaporation is consequently shifted to a lower vapor pressure compared to water in the wider pores.[2] The observed hysteresis is larger in the case of the hydrophobic samples than in the case of the hydrophilic ones. This is probably due to the difference in contact angle between adsorption and desorption. Indeed, in the first stages of the adsorption experiment, water molecules interact with the pristine wall surface. However, in the initiating desorption experiment, they draw back from a wet surface.[33,34] As the contact angle of the latter is smaller than that of the former in the case of the hydrophobic samples, large hysteresis is observed, according to the Kelvin equation for desorption, which takes analogue form to Equation 1 but considers a desorption pressure P_d, instead of a condensation pressure P_c. Thus, the equilibrium desorption pressure P_d also depends on the pore hydrophilicity.[33,34] Moreover, we observe that the filling and emptying of the pore is not totally reversible. This effect is clearly more acute in hydrophobic samples, which are more susceptible to chemical reactions with water upon the completion of condensation.

Conclusions

The modification of the PSi surfaces by oxidation and self-assembly of organosilanes allows controlling their wetting. Imaging the internal surface with high resolution (by HIM and TEM tomography) provided insight not only into the general columnar structure, but also into
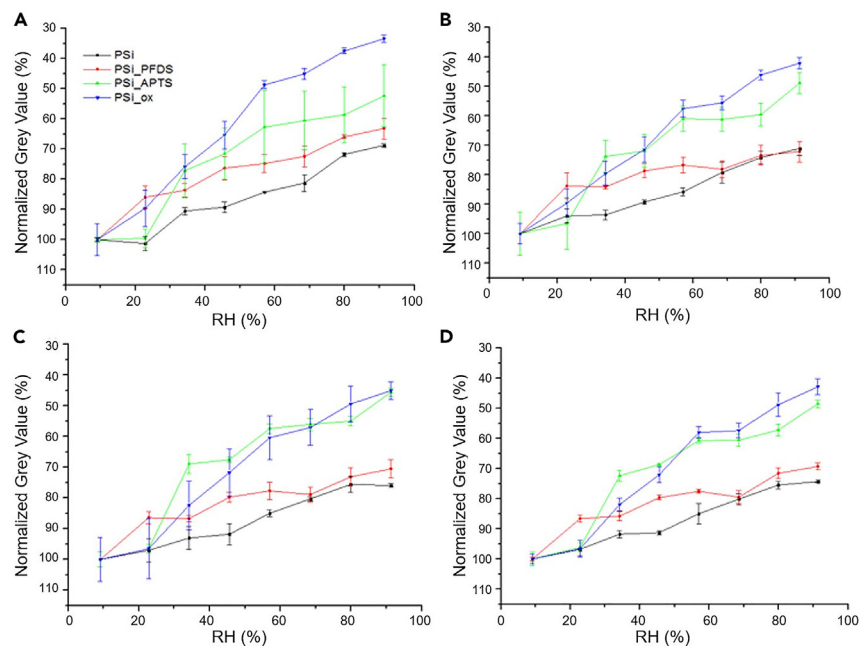
Figure 6. Evolution of grey value for increasing humidity for categorized pore sizes and chemistries
(A–D) Normalized gray value as a function of RH (%) for pores of (A) 20 nm, (B) 25 nm, (C) 30 nm and (D) 35 nm of diameter for the different PSi surfaces.

the ramified interconnections through pore walls. We used wetSTEM to observe, on a single-pore basis, the water filling of the pores, in function of RH from the pore profiles of the different samples. A statistical analysis allowed establishing differences in the wetting dynamics depending on the surface chemistry. In particular, the capability of water adsorption is larger in the case of the hydrophilic samples than in that of the hydrophobic samples. That shows that self-assembled monolayers can be used to alter and control the chemical nature of porous surfaces and consequently their wettability.

Most important is that our statistical analysis is based on data obtained from single pores. In this way, we were able to obtain water adsorption isotherms categorized by pore size ranges. On the one hand, we can explain how the global (averaged) isotherm is composed from local "single-pore isotherms"; on the other hand, our strategy is suitable for nanoscale fluid handling as in the smaller microfluidic setups, and even for single-pore devices.

Additionally, the global gravimetric measurement of the sorption isotherms gave us complete water adsorption/desorption isotherms. This allowed to obtain more precise information about the wetting of the PSi samples and the mechanism of water adsorption and desorption. We found that the amount of adsorbed water is larger in the case of peroxidized and APTS-functionalized PSi than that of as-formed and PFDS-functionalized PSi; confirming the data obtained by the wetSTEM analysis. This difference in the hydrophobic/hydrophilic properties of the PSi surfaces also plays an important role on the width of the hysteresis loop. This latter is enlarged by the hydrophobicity, as predicted by the Kelvin equation.

PSi remains a porous material with a wide spectrum of technological applications and is commonly integrated in sensors, catalytic systems, and drug delivery biomaterials, to cite a few. The current study suggests that lifetime and stability of the devices could be optimized by performing parallel studies of functionality and point or cyclic wetSTEM studies of PSi with the specific functionalization required by the desired application. A modification of the characteristic wetting trend in a dry to wet cycle could be related to the deviation or failure of the device characteristics.

STAR★METHODS

Detailed methods are provided in the online version of this paper and include the following:

- KEY RESOURCES TABLE
- RESOURCE AVAILABILITY
  - Lead contact
  - Materials availability
  - Data and code availability
- EXPERIMENTAL MODEL AND SUBJECT DETAILS
- METHOD DETAILS
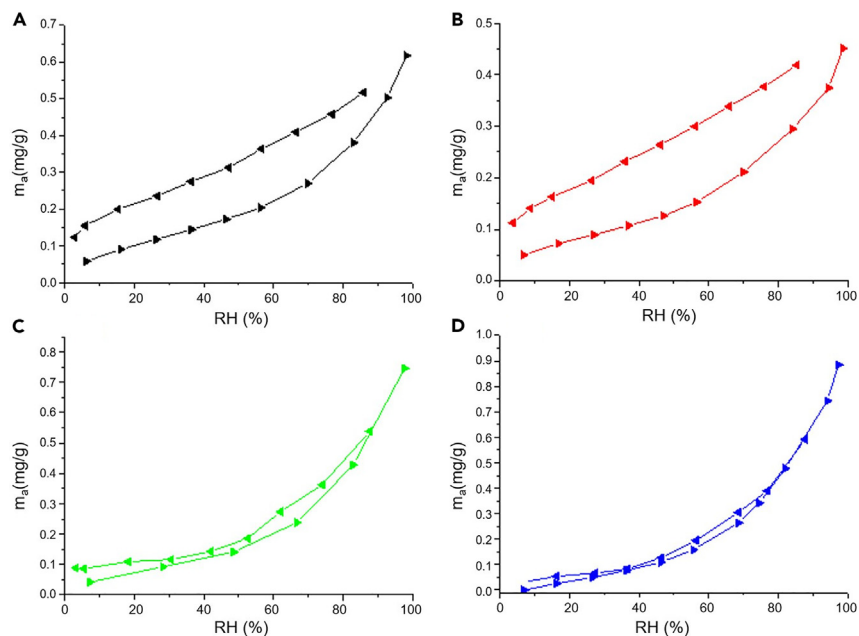
Figure 7. Water adsorption-desorption isotherms for the different PSi surface chemistries

(A–D) Water adsorption/desorption isotherms for (A) as-formed PSi, (B) PSi functionalized with PFDS, (C) functionalized with APTS, and (D) peroxidized PSi. ▶ Adsorption and ◀ desorption.

- ○ Preparation of thin porous silicon (PSi) layers and free-standing PSi
- ○ Functionalization of the PSi layers
- ○ Porous silicon structure: *In vacuo* imaging
- ○ Permeability experiments
- ○ WetSTEM experiments
- ● QUANTIFICATION AND STATISTICAL ANALYSIS
- ● ADDITIONAL RESOURCES

SUPPLEMENTAL INFORMATION

Supplemental information can be found online at https://doi.org/10.1016/j.isci.2023.107981.

AUTHOR CONTRIBUTIONS

C. Rodriguez participated in PSi synthesis and characterization, including wetting experiments, performed most of wetSTEM image analysis and produced a first draft version. V. Torres-Costa participated in PSi synthesis and reviewed all drafts. A.M. Bittner raised funds, conceived the wetting experiments, participated in the same and reviewed all drafts. S. Morin conceived the wetting experiments, participated in the same and reviewed all drafts. M. Cascajo Castresana participated in wetting experiments and reviewed all drafts. S. Chiriaev participated in He ion microscope characterization and reviewed all drafts. E. Modin and A. Chuvilin participated in tomographic and wetting characterization and reviewed all drafts. M Manso Silvan raised funds, conceived the characterization, participated in the same and reviewed all drafts.

DECLARATION OF INTERESTS

The authors declare no competing interests.

INCLUSION AND DIVERSITY

We worked to ensure gender balance in the recruitment of human subjects. We worked to ensure ethnic or other types of diversity in the recruitment of human subjects.

REFERENCES

1. Grünberg, B., Emmler, T., Gedat, E., Shenderovich, I., Findenegg, G.H., Limbach, H.H., and Buntkowsky, G. (2004). Hydrogen bonding of water confined in mesoporous silica MCM-41 and SBA-15 studied by H-1 solid-state NMR. Chem.–Eur. J. 10, 5689–5696. https://doi.org/10.1002/chem.200400351.

2. Pavlík, Z., Žumár, J., Medved, I., and Černý, R. (2012). Water Vapor Adsorption in Porous Building Materials: Experimental Measurement and Theoretical Analysis. Transp. Porous Media 91, 939–954. https://doi.org/10.1007/s11242-011-9884-9.

3. de la Llave, E., Molinero, V., and Scherlis, D.A. (2012). Role of Confinement and Surface Affinity on Filling Mechanisms and Sorption Hysteresis of Water in Nanopores. J. Phys. Chem. C 116, 1833–1840. https://doi.org/10.1021/jp206580z.

4. Kong, L., Sayem, H.M., and Tian, H. (2018). Influence of drying-wetting cycles on soil-water characteristic curve of undisturbed granite residual soils and microstructure mechanism by nuclear magnetic resonance (NMR) spin-spin relaxation time (T-2) relaxometry. Can. Geotech. J. 55, 208–216. https://doi.org/10.1139/cgj-2016-0614.

5. Shahraeeni, E., and Or, D. (2012). Pore-scale evaporation-condensation dynamics resolved by synchrotron x-ray tomography. Phys. Rev. 85, 016317. https://doi.org/10.1103/PhysRevE.85.016317.

6. An, R., Kong, L., Zhang, X., and Li, C. (2022). Effects of dry-wet cycles on three-dimensional pore structure and permeability characteristics of granite residual soil using X-ray micro computed tomography. J. Rock Mech. Geotech. Eng. 14, 851–860. https://doi.org/10.1016/j.jrmge.2021.10.004.

7. Verdaguer, A., Sacha, G.M., Bluhm, H., and Salmeron, M. (2006). Molecular structure of water at interfaces: Wetting at the nanometer scale. Chem. Rev. 106, 1478–1510. https://doi.org/10.1021/cr040376l.

8. Schmeltzer, J.M., and Buriak, J.M. (2004). Recent Developments in the Chemistry and Chemical Applications of Porous Silicon. In The Chemistry of Nanomaterials: Synthesis, Properties and Applications, C.N.R. Rao, A. Müller, and A.K. Cheetham, eds. (Wiley).

9. Sailor, M.J. (2011). Chemistry of Porous Silicon. In Porous Silicon in Practice, M.J. Sailor, ed. (Wiley), pp. 189–227. https://doi.org/10.1002/9783527641901.ch6.

10. Mareš, J., Krištofik, J., and Hulicius, E. (1995). Influence of humidity on transport in porous silicon. Thin Solid Films 255, 272–275. https://doi.org/10.1016/0040-6090(94)05670-9.

11. Kovacs, A., Meister, D., and Mescheder, U. (2009). Investigation of humidity adsorption in porous silicon layers. Phys. Status Solidi 206, 1343–1347. https://doi.org/10.1002/pssa.200881106.

12. Rittersma, Z.M., Splinter, A., Bödecker, A., and Benecke, W. (2000). A novel surface-micromachined capacitive porous silicon humidity sensor. Sens. Act. B Chem. 68, 210–217. https://doi.org/10.1016/s0925-4005(00)00431-7.

13. Xifré Pérez, E., Marsal, L.F., Ferré-Borrull, J., Trifonov, T., and Pallarès, J. (2007). Influence of the humidity conditions on the reflectivity spectrum of a porous silicon microcavity. Phys. E Low-dimens. Syst. Nanostruct. 38, 172–175. https://doi.org/10.1016/j.physe.2006.12.033.

14. Oswald, J., Mareš, J., Krištofik, J., and Sedlačík, R. (1996). Dependence of PS photoluminescence on relative humidity. Thin Solid Films 276, 268–271. https://doi.org/10.1016/0040-6090(95)08093-7.

15. Mandal, N.P., Dey, S., and Agarwal, S.C. (2004). Influence of surface treatments on nanocrystalline silicon. Thin Solid Films 451–452, 375–378. https://doi.org/10.1016/j.tsf.2003.11.068.

16. Xu, Z., Song, K., Yuan, S.L., and Liu, C.B. (2011). Microscopic Wetting of Self-Assembled Mono layers with Different Surfaces: A Combined Molecular Dynamics and Quantum Mechanics Study. Langmuir 27, 8611–8620. https://doi.org/10.1021/la201328y.

17. Szöri, M., Tobias, D.J., and Roeselová, M. (2009). Microscopic Wetting of Mixed Self-assembled Monolayers: A Molecular Dynamics Study. J. Phys. Chem. B 113, 4161–4169. https://doi.org/10.1021/jp8074139.

18. Bogner, A., Thollet, G., Basset, D., Jouneau, P.H., and Gauthier, C. (2005). Wet STEM: A new development in environmental SEM for imaging nano-objects included in a liquid phase. Ultramicroscopy 104, 290–301. https://doi.org/10.1016/j.ultramic.2005.05.005.

19. Donald, A.M. (2003). The use of environmental scanning electron microscopy for imaging wet and insulating materials. Nat. Mater. 2, 511–516. https://doi.org/10.1038/nmat898.

20. Bogner, A., Jouneau, P.H., Thollet, G., Basset, D., and Gauthier, C. (2007). A history of scanning electron microscopy developments: Towards "wet-STEM" imaging. Micron 38, 390–401. https://doi.org/10.1016/j.micron.2006.06.008.

21. Alonso, J.M., Tatti, F., Chuvilin, A., Mam, K., Ondarçuhu, T., and Bittner, A.M. (2013). The Condensation of Water on Adsorbed Viruses. Langmuir 29, 14580–14587. https://doi.org/10.1021/la4019376.

22. Tosatti, S., Michel, R., Textor, M., and Spencer, N.D. (2002). Self-assembled monolayers of dodecyl and hydroxy-dodecyl phosphates on both smooth and rough titanium and titanium oxide surfaces. Langmuir 18, 3537–3548. https://doi.org/10.1021/la011459p.

23. Muñoz-Noval, Á., Hernando Pérez, M., Torres Costa, V., Martín Palma, R.J., de Pablo, P.J., and Manso Silván, M. (2012). High Surface Water Interaction in Superhydrophobic Nanostructured Silicon Surfaces: Convergence between Nanoscopic and Macroscopic Scale Phenomena. Langmuir 28, 1909–1913. https://doi.org/10.1021/la2041289.

24. Yang, C.Y., Huang, L.Y., Shen, T.L., and Yeh, J.A. (2010). Cell adhesion, morphology and biochemistry on nano-topographic oxidized silicon surfaces. Eur. Cell. Mater. 20, 415–430.

25. Zhou, Y., Zhang, J., Wang, Z., He, F., Peng, S., and Li, Y. (2021). A modified TA-APTES coating: Endowing porous membranes with uniform, durable superhydrophilicity and outstanding anti-crude oil-adhesion property via one-step process. J. Membr. Sci. 618, 118703. https://doi.org/10.1016/j.memsci.2020.118703.

26. Moreno-Cerrada, D., Rodríguez, C., Moreno-Madrid, F., Selivanovitch, E., Douglas, T., de Pablo, P.J., and Manso Silván, M. (2019). Loading the dice: The orientation of virus-like particles adsorbed on titanate assisted organosilanized surfaces. Biointerphases 14, 011001. https://doi.org/10.1116/1.5077010.

27. Rodriguez, C., Laplace, P., Gallach-Pérez, D., Pellacani, P., Martín-Palma, R., Torres-Costa, V., Ceccone, G., and Manso Silván, M. (2016). Hydrophobic perfluoro-silane functionalization of porous silicon photoluminescent films and particles. Appl. Surf. Sci. 380, 243–248. https://doi.org/10.1016/j.apsusc.2016.01.119.

28. R.W. Cohn, ed. (2014). Freestanding Metallic and Polymeric Nanostructures: Direct Self-Assembly (Taylor & Francis).

29. Thommes, M. (2010). Physical Adsorption Characterization of Nanoporous Materials. Chem. Ing. Tech. 82, 1059–1073. https://doi.org/10.1002/cite.201000064.

30. Shirtcliffe, J.,N., and Roach, P. (2013). Superhydrophobicity for Antifouling Microfluidic Surfaces , bookTitle= Microfluidic Diagnostics: Methods and Protocols (Humana Press). https://doi.org/10.1007/978-1-62703-134-9_18.

31. Thommes, M., Smarsly, B., Groenewolt, M., Ravikovitch, P.I., and Neimark, A.V. (2006). Adsorption hysteresis of nitrogen and argon in pore networks and characterization of novel micro- and mesoporous silicas. Langmuir 22, 756–764. https://doi.org/10.1021/la051686h.

32. ALOthman, Z. (2012). A Review: Fundamental Aspects of Silicate Mesoporous Materials. Materials *5*, 2874–2902. https://doi.org/10.3390/ma5122874.

33. Factorovich, M.H., Gonzalez Solveyra, E., Molinero, V., and Scherlis, D.A. (2014). Sorption Isotherms of Water in Nanopores: Relationship Between Hydropohobicity, Adsorption Pressure, and Hysteresis. J. Phys. Chem. C *118*, 16290–16300. https://doi.org/10.1021/jp5000396.

34. Monson, P.A. (2008). Contact Angles, Pore Condensation, and Hysteresis: Insights from a Simple Molecular Model. Langmuir *24*, 12295–12302. https://doi.org/10.1021/la801972e.

35. Rodriguez, C., Ahumada, O., Cebrián, V., Torres Costa, V., and Manso Silván, M. (2018). Biofunctional porous silicon micropatterns engineered through visible light activated epoxy capping and selective plasma etching.

Vacuum *150*, 232–238. https://doi.org/10.1016/j.vacuum.2018.01.045.

36. Sano, H., Maeda, H., Matsuoka, S., Lee, K.H., Murase, K., and Sugimura, H. (2008). Self-assembled monolayers directly attached to silicon substrates formed from 1-hexadecene by thermal, ultraviolet, and visible light activation methods. Jpn. J. Appl. Phys. *47*, 5659–5664. https://doi.org/10.1143/jjap.47.5659.

STAR★METHODS

KEY RESOURCES TABLE

REAGENT or RESOURCE	SOURCE	IDENTIFIER
Chemicals, peptides, and recombinant proteins		
p-type boron-doped	ITME, Poland	CAS: 7440-21-3
Hydrofluoric Acid 48%	Sigma-Aldrich, Spain	CAS: 7664-39-3
Absolute Ethanol	Sigma-Aldrich, Spain	CAS: 64-17-5
Aminopropyltriethoxysilane	Sigma-Aldrich, Spain	CAS: 919-30-2
Perfluorodecylsilane	Sigma-Aldrich, Spain	CAS: 101947-16-4
Hydrogen Peroxide 30%	Sigma-Aldrich, Spain	CAS: 7722-84-1
Phosphotungstic acid hydrate	Sigma-Aldrich, Spain	CAS: 12501-23-4
Software and algorithms		
ImageJ	NIH	imagej.net/ij/index.html
MATLAB	MathWorks	es.mathworks.com/

RESOURCE AVAILABILITY

Lead contact

Further information and requests for resources should be directed to the lead contact, Miguel Manso Silván (miguel.manso@uam.es).

Materials availability

No new or unique materials or reagents were generated in this study.

Data and code availability

- All data reported in this paper will be shared by the lead contact upon request.
- No code was developed for data acquisition or analysis. All data processing was developed with mentioned software applications and available plug-ins.
- Any additional information required to reanalyze the data reported in this paper is available from the lead contact upon request.

EXPERIMENTAL MODEL AND SUBJECT DETAILS

Our study does not use experimental models typical in the life sciences.

METHOD DETAILS

Preparation of thin porous silicon (PSi) layers and free-standing PSi

The back side of p-type boron-doped (resistivity 0.01–0.02 Ωcm) (100)-oriented silicon wafers was first coated with an aluminum layer to provide low resistance ohmic electrical contacts, and subsequently cut into 15 mm × 15 mm pieces, which were mounted on a Teflon[(R)] two-electrode electrochemical cell. The silicon wafer was the anode, and a platinum filament network was used as the cathode. An Agilent 6634B DC power supply was used to control the current. A columnar PSi layer was then fabricated by electrochemical etching of the silicon wafer in an electrolyte composed of a mixture of hydrofluoric acid (HF) (40%) and absolute ethanol (volume ratio 1:2). We employed a current of 80 mA/cm^2 for 20 s to create a 2000 $\pm$ 20 nm thick PSi structure. These were then rinsed with ethanol and dried with nitrogen. These samples are in the following referred to as freshly hydrolyzed PSi, H-PSi. To create the free-standing PSi layers, the anodization was followed by a pulse of 5 s at 407 mA/cm^2 to delaminate the PSi from the silicon substrate. The free-standing layers were removed from the electrolyte, washed with pure ethanol and transferred to a copper TEM grid.

Functionalization of the PSi layers

The free-standing PSi layers and the PSi layers on silicon were functionalized with aminopropyl triethoxysilane (APTS, terminated by an amine group, NH_2) and with 1H,1H,2H,2H-perfluorodecyl triethoxysilane (PFDS) (both from Sigma Aldrich). Each organosilane was dissolved in ethanol (0.2%), and PSi was incubated in this solution for 10 min and 30 min, respectively, under white light illumination (150 W halogen

lamp) at room temperature.[35,36] The silane concentration used for the functionalization is very low to remain in the submonolayer regime. The resulting targeted samples are labeled as APTS-PSi and PFDS-PSi, respectively. Aside from the functionalization, we also oxidized the PSi thin layers in a mixture of aqueous H_2O_2 (30% wt) and absolute ethanol (1:1) for 30 min, and then rinsed in ethanol. This procedure results in hydroxyl groups at the surface; the samples are named OH-PSi in the following. All chemical functionalization steps were carried out in a glovebox filled with nitrogen.

Porous silicon structure: *In vacuo* imaging

A pre-characterization of the pore structure of free-standing PSi was performed by using Field Emission SEM (FESEM), helium ion microscopy (HIM) and TEM. The TEM was a JEOL 2100F, operated at 200 kV. FESEM images were recorded with a Philips XL30S microscope operated at 10 keV. High resolution imaging of the samples was performed with a Zeiss Orion NanoFab HIM. HIM imaging principles are like those of SEM. Only, instead of an electron beam, a He^+ ion beam is scanned over the sample surface and generates the secondary electrons used as imaging signal. The Zeiss instrument employs a Gas-Field-Ion Source and electrostatic optics for generation of a focused beam of helium ions. Compared to SEM, this technology is characterized by a superior resolution (about 0.3 nm), higher surface sensitivity and extreme focus depth, all of which are of great relevance for studies of mesoporous structures.

To visualize cross-sections of the porous layers, the specimens for HIM studies were cleaved from the wafer samples and fixed on metallic sample holders with an electrically conductive silver paste to ensure an effective charge removal during imaging. Just before imaging, the sample chamber and the sample stage were cleaned with an Evactron plasma cleaner to remove possible hydrocarbon contaminations inside the chamber, which can deteriorate image quality.

Permeability experiments

To study the water permeability of PSi and of the modified PSi samples, we dissolved phosphotungstic acid (PTA) in water (2%) and placed a droplet on the surface of the PSi layer on silicon wafer samples. Once the droplet had evaporated, we cut the sample by focused ion beam (FIB) slicing (see below) to observe the cross-section by FESEM.

FIB slicing and 3D imaging was performed using a dual-beam system FIB/SEM (FEI Helios 450S Dual Beam). The PSi samples, pre-coated with a 150 nm Pt protective layer, were sectioned parallel to the surface, removing the surface layers stepwise with the Ga ion FIB, operated at 30 kV and 18 pA. Images for each section were successively acquired by SEM (accelerating voltage from 2 to 5 kV; current: 100 to 200 pA) with various detectors. Especially useful was the backscattering detector, which provides high contrast for PTA-rich material. The target slice thickness was set to 20 nm, the voxel size to $2.8 \times 2.8 \times 20$ nm^3. The process was run in fully automated mode, using the AutoSlice&View G3 software. The thus acquired 3D data was further processed, visualised and quantified in FEI VSG Avizo software.

The surface wettability of PSi and flat model samples was evaluated with a water contact angle goniometer (KSV CAM-101) used in the static sessile drop mode: a 3 μL drop of water was applied onto the sample surface and the contact angle formed with the surface was measured. Each measurement was repeated five times.

WetSTEM experiments

Dynamic experiments involving condensation and evaporation of water on PSi were carried out with a FEI QUANTA 250FEG with a wetSTEM setup. This enables STEM imaging through a standard TEM copper grid, mounted on a Peltier stage. Thin free-standing PSi samples were placed on the grid, with the pores oriented parallel to the electron beam (vertically). The wetSTEM detector is integrated in the Peltier stage; it comprises a disk (bright field mode) and a ring (dark field mode) detector. The chamber pressure was varied from the base pressure of $\approx 10^{-4}$ Pa up to >1000 Pa water vapor, supplied through an automated valve. An increase in pressure was achieved by introducing water vapor through a leak valve. A decrease was achieved instead by pumping. To prevent premature evaporation from, and condensation on the sample, an optimized pump down sequence was used (several cycles of water vapor filling at up to 1000 Pa and pumping down to ≈ 100 Pa at ambient sample temperature).

We used a beam voltage of 20 kV, with an electron beam spot of about 13 nm (spot size 3). The dose, and thus the beam damage, was reduced by working at the minimal column aperture. The sample temperature was maintained at 5°C (water vapor saturation pressure 866 Pa), and the relative humidity (RH) was increased/decreased by increasing/decreasing the chamber pressure, with sufficient time to reach a steady state. To avoid beam damage, low magnification was used throughout the experiment (several hours), except for acquiring the final images (a few min in total). Hence, each image corresponds to a short zoom-in event.

The results were correlated with water adsorption measurements for the different PSi samples (PSi layer on silicon wafer samples) at 25°C, reaching a total pressure of 2338 Pa, performed with an automatic vapor adsorption apparatus (Belsorp-Aqua, co. Rubotherm/Bel), using the volumetric gas adsorption method.[11]

QUANTIFICATION AND STATISTICAL ANALYSIS

To account for variations of the contrast and brightness with changing vapor pressure and to evaluate a greyscale information on the image quantitatively, we have normalized the gray levels on every image. First, the values of contrast and brightness of the detector in BF mode were selected so that images were not saturated either in black or white in the whole range of utilized pressures. Second, for every acquiring condition the images were normalized to the contrast range between intensity at the large holes (100% transmission) and intensity at the position

of the cupper grid (0% transmission) at these conditions. This contrast setting was not changed during zooming in, and during images acquisition.

Quantification from TEM images was performed with ImageJ software. The required basic statistical calculations (pore size distribution, mean values of gray scale and standard deviations) and plots were performed with MATLAB.

ADDITIONAL RESOURCES

No relevant additional resources have been used to carry out this work.